

Large-scale DFT calculations of multi-component glass systems $(\text{SiO}_2)_{0.70}(\text{Al}_2\text{O}_3)_{0.13}(\text{XO})_{0.17}$ ($X = \text{Mg}, \text{Ca}, \text{Sr}, \text{Ba}$): Accuracy of classical force fields

Atsushi Tanaka^{a,*}, Atsuki Saito^a, Takashi Murata^a, Ayako Nakata^b, Tsuyoshi Miyazaki^b

^a Research and Development Group, Nippon Electric Glass Co., Ltd., 2-7-1 Seiran, Otsu, Shiga 520-8639, Japan

^b Research Center for Materials Nanoarchitectonics (MANA), National Institute for Materials Science (NIMS), 1-1 Namiki, Tsukuba, Ibaraki 305-0044, Japan

ARTICLE INFO

Keywords:

Multi-component glass
First-principles calculations
Large-scale DFT
Classical force fields
Molecular dynamics simulations

ABSTRACT

Although molecular dynamics (MD) simulation is a powerful tool for investigating the atomic-scale structures of complex materials, several challenges limit their reliable and accurate application to multi-component glass systems. The available force fields (FFs) that can treat many elements in a multi-component glass are limited, and even if such a FF exists, its accuracy is suspicious due to the large variety and complexity of chemical environments in these materials. First-principles calculations based on the density functional theory (DFT) are reliable, but prohibitively expensive with conventional methods. In this study, we use large-scale DFT techniques and demonstrate that it is possible to perform efficient and accurate DFT calculations of multi-component glass systems, such as $(\text{SiO}_2)_{0.70}(\text{Al}_2\text{O}_3)_{0.13}(\text{XO})_{0.17}$ ($X = \text{Mg}, \text{Ca}, \text{Sr}, \text{Ba}$), containing about 1000–5000 atoms. From the results of large-scale DFT calculations, we evaluate the accuracy of some classical FFs, and show that the accuracy for non-bridging oxygen atoms is very low especially when the Si–O distance is short. Large differences in the distribution of Si–O–Si angles observed in the FF-MD and DFT-MD simulations and the unique electronic structure in the case of $X = \text{Mg}$ are also discussed.

1. Introduction

Commercial glass products have improved the quality of everyday life. Most products are made of multi-component glasses, and their compositions vary depending on their roles. For example, soda-lime glasses are used for windows because of transparency and high production efficiency. Some glass fibers are made of alkaline earth aluminoborosilicate glass for high insulations [1]. Cover glass sheets for electric devices are made of alkaline-containing silica glasses, which can be ion-exchanged to strengthen their surfaces.

The advantage of mixing several components is the improvement of the characteristic properties of glass. However, the mechanisms to improve these properties are still unclear and several possible mechanisms have been proposed so far. The glasses are random-network materials and it makes difficult to obtain the detailed atomic-scale structures from experiments. Zachariasen [2] proposed a set of rules on network structures of vitreous silica and complex glasses. Based on Zachariasen's model and experimental results of X-ray scattering, neutron scattering and NMR, the structures of vitreous silica and some binary glasses have been clarified to some extent. For example, the medium-range structural order of vitreous silica was investigated [3],

and the effects of adding alkali-oxides on silica tetrahedral network were observed [4], which revealed that alkali-oxides break silicon-oxygen bonds and generate non-bridging-oxygen (NBO) atoms. As the number of NBO atoms increases, silica cannot maintain stable 3D networks, and the viscosities are expected to decrease.

These experimental approaches to glass structures are very useful for single or binary glass systems. Similar approaches were also applied to multi-component glasses [5], but it was found that the structures are more complex when other oxides, such as aluminum, boron, alkali, or alkali earth oxides are added. Because of the complexity and many variations of the coordination properties, experimental analyses of the multi-component glasses are challenging, compared with that single or binary glass systems.

To remedy the difficulties in the experimental analyses, computational approaches are useful. Molecular dynamics (MD) simulations have been used to predict structures and characteristic properties of glasses. Some classical force-fields (FF) [6–8] are designed for multi-component glasses as well. However, the reliability of such classical FF is often uncertain, since the experimental information is limited. It is expected that first-principles calculations based on the density

* Corresponding author.

E-mail addresses: atstanaka@neg.co.jp (A. Tanaka), MIYAZAKI.Tsuyoshi@nims.go.jp (T. Miyazaki).

<https://doi.org/10.1016/j.jnoncrysol.2023.122714>

Received 23 May 2023; Received in revised form 29 September 2023; Accepted 31 October 2023

Available online 25 November 2023

0022-3093/© 2023 The Authors. Published by Elsevier B.V. This is an open access article under the CC BY license (<http://creativecommons.org/licenses/by/4.0/>).

functional theory (DFT) can solve this problem, because they provide reliable and accurate information even for unknown materials. There are several attempts to develop reliable FFs, including the recent machine-learning FFs, from the first-principles calculations of silicate glass or melt systems at various conditions [9–15]. Recently glass structures simulated using DFT-MD were reported to be more reliable than those using classical FFs [16,17]. Although DFT studies of multi-component glass systems are potentially useful, the difficulty is that large systems containing many atoms are needed to reproduce the irregular network structure with medium range order. The computational cost of DFT calculations is expensive, especially when the number of atoms is larger than 1000 [18]. Although there are already some examples of large scale DFT calculations that clarify the complex structures of glass systems [19,20], there are only a few reports of the DFT study of multi-component glasses [16,17,21,22], which generally need more atoms compared with single or binary glass systems.

In this study, we use large-scale DFT techniques implemented in the large-scale and linear-scaling DFT code CONQUEST to study the accuracy of classical FFs for multi-component glasses. We demonstrate that reliable and accurate DFT calculations of multi-component glass systems, $(\text{SiO}_2)_{0.70}(\text{Al}_2\text{O}_3)_{0.13}(\text{XO})_{0.17}$ ($X = \text{Mg, Ca, Sr, Ba}$), containing about 5000 atoms are possible using a large-scale DFT technique called the multisite method. A comparison of the structures from the DFT-MD and FF-MD simulations and the analysis of the electronic structure of $(\text{SiO}_2)_{0.70}(\text{Al}_2\text{O}_3)_{0.13}(\text{XO})_{0.17}$ are also provided.

The rest of the paper is organized as follows: In Section 2, an overview of large-scale DFT techniques and the accuracy of the basis set used in the DFT calculations are provided. The classical FFs employed in this study and the preparation method to generate the snapshot structures for benchmark tests are also explained. In Section 3, the results of benchmark tests and large-scale DFT calculations of multi-component glass systems are presented. A summary of the results is given in Section 4.

2. Computational methods

2.1. Classical force fields

In this study, three kinds of potentials are used for the classical FFs. The first was proposed by Pedone et al. [6], called FF-Pedone hereafter. Its potential is expressed as:

$$U_{ij}(r) = D_{ij}[\{1 - e^{-a_{ij}(r-r_0)}\}^2 - 1] + \frac{C_{ij}}{r^{12}} + \frac{z_i z_j e^2}{4\pi\epsilon_0 r}, \quad (1)$$

where, r is the distance between atoms i and j . The first, second, and third terms represent the short-range Morse function, repulsive contribution, and long-range Coulomb potential, respectively. For comparison, we also used two other FFs that carry different sets of Buckingham type parameters, as shown in Eq. (2); proposed by Deng et al. [7], and Wang et al. [8], referred to as FF-Deng and FF-Wang, respectively.

$$U_{ij}(r) = A_{ij} \exp\left(-\frac{r}{\rho_{ij}}\right) - \frac{C_{ij}}{r^6} + \frac{z_i z_j e^2}{4\pi\epsilon_0 r}, \quad (2)$$

where the first, second, and third terms represent the short-range electronic repulsion, van der Waals interactions, and long-range Coulomb potential. The Buckingham type potential is known to have drawbacks in the short range contact region; therefore, the first and second terms in Eq. (2) are replaced by other FFs. The parameters of these FFs are provided in Supplementary.

2.2. Large-scale DFT methods

2.2.1. Local basis sets and support functions

In the large-scale DFT code CONQUEST[23–26], the Kohn–Sham orbitals for the state n , $\psi_n(\mathbf{r})$, or the density matrix $\rho(\mathbf{r}, \mathbf{r}')$ are expressed by local functions around each atom i with the orbital α , $\phi_{i\alpha}(\mathbf{r})$,

called support functions. The Kohn–Sham orbitals can be obtained by diagonalizing the Hamiltonian matrix,

$$H_{i\alpha,j\beta} = \int d\mathbf{r} \phi_{i\alpha}(\mathbf{r}) \hat{H} \phi_{j\beta}(\mathbf{r}) \quad (3)$$

with the overlap matrix, since the support functions are not orthogonal in general. In Eq. (3), \hat{H} is the Kohn–Sham Hamiltonian operator using the pseudopotential method. For the exchange–correlation term in the DFT, the generalized gradient approximation (GGA) with the Perdew–Burke–Ernzerhof (PBE) functional [27] was used throughout this study. Although it was reported that dispersion corrections can improve the energetics among the various polymorphs of SiO_2 [28], we have confirmed that the effects of the empirical dispersion corrections [29] on the atomic forces in the present glass systems were almost negligible and the corrections were not considered in this study.

When considerably large systems containing more than a few tens of thousands of atoms need to be calculated, a linear-scaling mode is used with the density matrix minimization method. In the linear-scaling mode, the density matrix, $\rho(\mathbf{r}, \mathbf{r}')$, is optimized to minimize the DFT total energy without calculating the Kohn–Sham orbitals.

The support functions themselves are represented in terms of one of two basis sets: the pseudo atomic orbitals (PAOs); and blip functions [30]. In this study, we use PAOs as a basis set, which are generated by the MAKEIONFILES code provided in the CONQUEST package [31], using the pseudopotentials generated by ONCVSP code [32, 33] with the parameters given in PSEUDO.DJVO[34,35]. The support functions of atom i are usually expressed by a linear combination of the PAOs of the atom, as shown in Eq. (4):

$$\phi_{i\alpha}(\mathbf{r}) = \sum_{\mu} c_{i\alpha}(\mu) \chi_{i\mu}(\mathbf{r}), \quad (4)$$

where $\chi_{i\mu}(\mathbf{r})$ is the PAO of the orbital μ of the atom i . It is also possible to use a PAO for each support function (primitive basis set). Although a systematic convergence is difficult with the PAO basis set, the accuracy of the calculations can be improved if the number of orbitals is increased and the basis set of double-zeta plus polarization functions (DZP) is accurate enough in most cases [36–38].

Table 1 shows the optimized lattice parameters and bulk modulus calculated with the DZP basis sets for SiO_2 , Al_2O_3 , MgO , CaO , SrO and BaO . The results show that the optimized structures are similar to those obtained using other DFT calculations, confirming that the DZP basis sets used herein are accurate enough for these oxides. Therefore, we used the DZP basis sets throughout this study.

2.2.2. Multisite method for large-scale DFT calculations

Since the computational cost (CPU time) to diagonalize the Hamiltonian in Eq. (3) scales with the cubic of the number of support functions, it is essential to decrease the number of support functions to reduce the cost of the calculations for large-scale systems. Note that the cost in the linear-scaling calculations is also proportional to the cube of the number of support functions. If we are to express the support functions in Eq. (4), we need at least one support function for each angular momentum [37]. However, if we construct the support functions as the linear-combination of PAOs on a target atom, as well as its neighboring atoms, defined by a cutoff radius R_{MS} ,

$$\phi_{i\alpha}(\mathbf{r}) = \sum_k^{\text{neighbours}} \sum_{\mu \in k} C_{i\alpha}(k\mu) \chi_{k\mu}(\mathbf{r}). \quad (5)$$

Then, the number of support functions can be reduced to that of a minimal basis set [42,43]. Here, $\chi_{k\mu}$ is a PAO of its neighboring atoms k (including i itself) with the orbital μ and the support functions are thus called multisite support functions (MSSFs).

In CONQUEST, two methods have been implemented to determine the linear-combination coefficients of MSSFs. One of the methods is local-filter-diagonalisation (LFD) proposed by Rayson and Briddon [42, 44,45], and the other is numerical optimization [43]. In the LFD

Table 1

Optimized lattice parameters and bulk modulus for various oxides calculated with the DZP basis set. Experimental values are also presented for comparison. SiO_2 (α -quartz) and $\alpha\text{-Al}_2\text{O}_3$ have hexagonal symmetry, while the other four oxides have a cubic (NaCl) structure.

	SiO_2 (α -quartz)	Al_2O_3 ($\alpha\text{-Al}_2\text{O}_3$)	MgO	CaO	SrO	BaO
Lattice parameter: a_{opt} , c_{opt}	4.90, 5.39	4.74, 13.13	4.28	4.85	5.21	5.61
Lattice parameter: a_{exp} , c_{exp}	4.92, 5.41 ^a	4.67, 12.95 ^b	4.22 ^c	4.82 ^c	5.16 ^c	5.52 ^c
Bulk modulus : opt (GPa)	46.6	230.6	148.6	112.1	81.2	65.3
Bulk modulus : exp (GPa)	38 ^a	264 ^b	160 ^c	111 ^c	89 ^c	74 ^c

^a Ref. [39].

^b Ref. [40].

^c Ref. [41].

method, local molecular orbitals are first calculated by solving the local Hamiltonian of a cluster comprising of the atoms within the range of R_{LFD} from a target atom. Subsequently, the linear-combination coefficients are obtained by projecting the occupied local molecular orbitals onto trial vectors which are localized around the target atom. When using the LFD method, the R_{MS} should be equal or shorter than the subspace region in the LFD method R_{LFD} . On the other hand, the linear-combination coefficients are directly optimized to minimize the total energy in the numerical optimization method. When the numerical optimization method is used, the LFD method is first employed to obtain the initial guess of the linear-combination coefficients. If both R_{LFD} and R_{MS} are large, these two methods would result in almost the same accuracy. Since the MSSFs depend on the charge density of the system, which in turn depends on the MSSFs, the linear-combination coefficients need to be determined self-consistently [42].

The accuracy of the MSSFs depends on the R_{MS} and the calculations with MSSF can reproduce the accuracy of the primitive PAO basis set if R_{MS} is large enough. One of the advantages is that the difference between the MSSF and primitive basis set calculations decreases exponentially not only in gapped systems, but also in metallic systems. In Section 3.2, we investigate the accuracy of MSSF calculations in the multi-component glass systems and show that accurate DFT calculations of about 5000-atom systems are possible with the MSSF method.

The reduction of the computational cost by the MSSF method is significant in the calculations of large systems, for which the cost of the LFD becomes negligible compared with the cost of diagonalizing $H_{i\alpha,j\beta}$ in Eq. (3). The number of DZP basis functions for Si or O is 13, while the number of their support functions in the MSSF method is 4. As a result, the reduction of the required memory size and cpu time by the MSSF method is estimated to be about 10.5 ($= (13/4)^2$) and 34 ($= (13/4)^3$) folds, respectively. For more accurate basis sets, such as TZTP, the reduction rate is even higher: 45 for memory requirement and 308 for the computational time.

2.2.3. Modeling of the glass structures by melt-quench process

The glass structures are generated by the MD simulations of melt-quench processes using classical FFs with the LAMMPS package. For all MD simulations, the time step is fixed at 1.0 fs. The initial atomic positions for FF-Pedone and FF-Deng are generated by random numbers, while the structure made by the melt-quench process with FF-Pedone in the following paragraph, is used as the initial structure for the model with FF-Wang to prevent the so-called Buckingham catastrophe. The size of the simulation cells for the initial structures with FF-Pedone and FF-Deng are determined by the experimental densities. In Section 3.1, three systems are investigated for the benchmark test of the classical FFs; pure SiO_2 (vitreous silica), $(\text{SiO}_2)_{0.5}(\text{Al}_2\text{O}_3)_{0.5}$, and $(\text{SiO}_2)_{0.5}(\text{CaO})_{0.5}$. The experimental densities of the three systems are reported to be 2.20, 2.74 [46,47] and 2.90 [48] g/cm³, respectively. These values at room temperature are calculated using the Archimedes method.

In the melt-quench process with FF-Pedone, the glass systems are first melted at 6000 K for 500 ps using the NVT ensemble. Subsequently, they are cooled down to 300 K at a rate of 5 K/ps in the

NVT simulation. After cooling, they are relaxed for 200 ps in the NVT simulations at 300 K. In the case of FF-Deng, the systems are first equilibrated at 300 K for 60 ps, then melted at 6000 K for 100 ps, and equilibrated at 5000 K for 100 ps. Following the equilibration of the liquid state, the systems are cooled down to 300 K at a cooling rate of 5 K/ps. These processes were conducted using the NVT simulations. Subsequently, the systems were relaxed at 300 K for 60 ps in the NPT ensemble at zero pressure, followed by the NVT simulations at 300 K for 60 ps. Regarding the process with FF-Wang, the systems are first melted at 3000 K for 10 ps in the NVT simulations, followed by the NPT simulations at 3000 K and zero pressure for 100 ps. They are cooled down to 300 K at a cooling rate of 1 K/ps in the NPT simulations at zero pressure. Finally, they are relaxed at 300 K for 100 ps in the NPT simulations at zero pressure, then NVT simulations at 300 K for 100 ps.

The densities of the glass structures generated with FF-Deng and FF-Wang are 2.29 and 2.47 g/cm³ for vitreous silica, 2.77 and 3.03 g/cm³ for $(\text{SiO}_2)_{0.5}(\text{Al}_2\text{O}_3)_{0.5}$, and 2.88 and 3.00 g/cm³ for $(\text{SiO}_2)_{0.5}(\text{CaO})_{0.5}$, respectively. The results agree with the experimental values for the structures made using the FF-Deng process. The densities of the structures made using the FF-Wang process are higher than the experimental values by about 10% for the first two systems, but the densities agree much better for $(\text{SiO}_2)_{0.5}(\text{CaO})_{0.5}$. Note that only NVT ensemble simulations are used in the melt-quench processes with FF-Pedone, and the experimental densities cannot be reproduced using NPT simulations.

3. Results

3.1. Benchmark tests for classical force fields in vitreous silica and binary glasses

In this section, we investigate the accuracy of the three types of classical FFs, FF-Pedone, FF-Deng and FF-Wang, explained in Section 2.1, for vitreous silica and binary glasses. Three systems were used for the benchmark tests; pure SiO_2 (vitreous silica), $(\text{SiO}_2)_{0.5}(\text{CaO})_{0.5}$, and $(\text{SiO}_2)_{0.5}(\text{Al}_2\text{O}_3)_{0.5}$. The number of atoms is 999 for vitreous silica and 1000 for the two binary glass systems. The snapshot structures were prepared by the melt-quench processes, explained in Section 2.2.3. Self-consistent DFT calculations were performed using a randomly selected snapshot structure for each system and for each FF. The calculated atomic forces by DFT, \vec{F}_{DFT} , were compared with those by classical FFs, \vec{F}_{FF} , and the three components of the atomic forces on the Si and O atoms in the vitreous silica system are plotted in Fig. 1(a) and (b), respectively. Fig. 1(c) and (e) show the forces on O and Ca atoms, respectively, in $(\text{SiO}_2)_{0.5}(\text{CaO})_{0.5}$, while Fig. 1(d) shows the forces on Al atoms in $(\text{SiO}_2)_{0.5}(\text{Al}_2\text{O}_3)_{0.5}$. The correlation coefficient, R , and the mean absolute deviation (MAD) between the atomic forces calculated by the three FFs and DFT are presented in Table 2.

The tendencies of the atomic forces on Si, Al, and Ca are shown in Fig. 1(a), (d), and (e). The forces on these atoms calculated by FF-Pedone qualitatively agree with those by DFT, although the amplitude of the forces by FF-Pedone is systematically underestimated, resulting in the high R value with large MAD values. FF-Deng basically shows a similar behavior with FF-Pedone. The agreement is a little better in vitreous SiO_2 , worse in $(\text{SiO}_2)_{0.5}(\text{Al}_2\text{O}_3)_{0.5}$, and very similar in

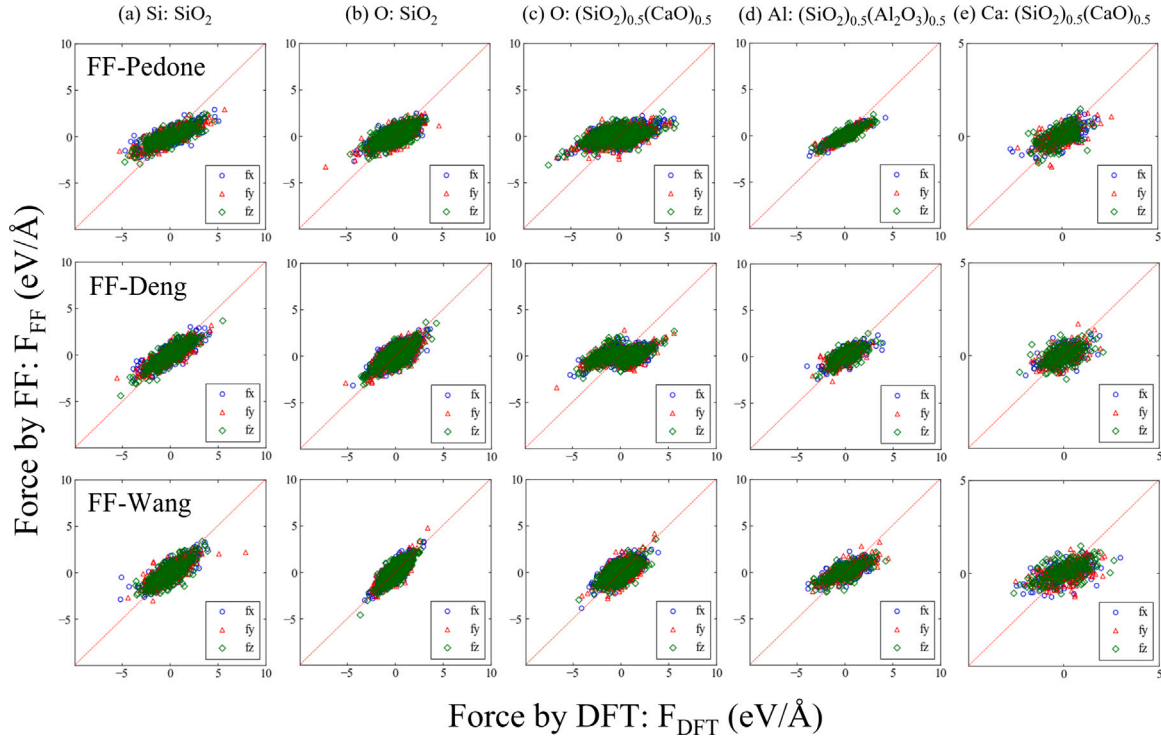


Fig. 1. Comparison of the components of atomic forces calculated by classical force fields \vec{F}_{FF} and DFT \vec{F}_{DFT} , for (a) Si and (b) O atoms in SiO_2 , (c) O atoms in $(\text{SiO}_2)_{0.5}(\text{CaO})_{0.5}$, (d) Al atoms in $(\text{SiO}_2)_{0.5}(\text{Al}_2\text{O}_3)_{0.5}$, and (e) Ca atoms in $(\text{SiO}_2)_{0.5}(\text{CaO})_{0.5}$. Three types of classical force fields, FF-Pedone, FF-Deng and FF-Wang are investigated.

Table 2

Correlation coefficient R and the mean absolute deviation (MAD) between the atomic forces calculated by classical force fields and DFT.

	FF-Pedone		FF-Deng		FF-Wang	
	R	MAD	R	MAD	R	MAD
Si: SiO_2	0.798	0.913	0.836	0.657	0.780	0.680
O: SiO_2	0.675	0.717	0.712	0.657	0.771	0.471
Si: $(\text{SiO}_2)_{0.5}(\text{Al}_2\text{O}_3)_{0.5}$	0.866	0.791	0.730	0.956	0.648	1.105
O: $(\text{SiO}_2)_{0.5}(\text{Al}_2\text{O}_3)_{0.5}$	0.727	0.655	0.554	0.801	0.772	0.493
Al: $(\text{SiO}_2)_{0.5}(\text{Al}_2\text{O}_3)_{0.5}$	0.880	0.515	0.717	0.586	0.727	0.796
Si: $(\text{SiO}_2)_{0.5}(\text{CaO})_{0.5}$	0.811	0.918	0.832	0.643	0.721	0.841
O: $(\text{SiO}_2)_{0.5}(\text{CaO})_{0.5}$	0.464	1.295	0.435	1.211	0.610	0.669
Ca: $(\text{SiO}_2)_{0.5}(\text{CaO})_{0.5}$	0.613	0.436	0.518	0.434	0.526	0.594

$(\text{SiO}_2)_{0.5}(\text{CaO})_{0.5}$. Using FF-Wang, the agreement with DFT forces in vitreous silica is worse than those of the other two FFs. In addition, agreements in Ca atoms by these FFs are worse than those for other elements in common.

For the atomic forces on oxygen atoms, these three FFs show rather different accuracies. As seen in Fig. 1(b) and (c), the agreement is very different between vitreous silica and $(\text{SiO}_2)_{0.5}(\text{CaO})_{0.5}$ when using FF-Pedone or FF-Deng. The agreement in the case of $(\text{SiO}_2)_{0.5}(\text{CaO})_{0.5}$ is much worse, as can be seen in Table 2. On the other hand, with FF-Wang, such a large difference cannot be seen between oxygen atoms in vitreous silica and those in $(\text{SiO}_2)_{0.5}(\text{CaO})_{0.5}$. Although it is difficult to judge which FF is more accurate in general, the three classical FFs evidently have different characteristics, especially for the oxygen atoms.

Aiming to clarify the conditions where \vec{F}_{FF} deviates significantly from \vec{F}_{DFT} for oxygen atoms, the comparison of the forces depending on the distance is investigated. Fig. 2 shows $|\vec{F}_{\text{FF}}|$, $|\vec{F}_{\text{DFT}}|$, and $|\Delta\vec{F}|$ ($\Delta\vec{F} = \vec{F}_{\text{FF}} - \vec{F}_{\text{DFT}}$) for the oxygen atoms in $(\text{SiO}_2)_{0.5}(\text{CaO})_{0.5}$. Here, the oxygen atoms are classified into bridging oxygen (BO) and NBO atoms. Usually, Ca atoms exist near the NBO atom, on the other side of the O-Si bond. In Fig. 2, the horizontal axis denotes the interatomic distance between an oxygen atom and its nearest neighboring atom. For FF-Pedone and FF-Deng, the results show that the deviations between

FF and DFT forces, $|\Delta\vec{F}|$, for NBO atoms are larger than those for BO atoms, implying that the accuracy of the FFs for NBO atoms is much worse compared with the one for BO atoms. The deviation is especially large when the bond length of NBO atoms is shorter than 1.6 Å. In contrast, such large differences between NBO and BO atoms are not observed in the atomic forces calculated by FF-Wang. Furthermore, the agreement with the DFT forces is better when using FF-Wang, in the case of $(\text{SiO}_2)_{0.5}(\text{CaO})_{0.5}$, compared with FF-Pedone and FF-Deng. These results suggest that FF-Pedone and FF-Deng tend to underestimate the repulsive potential for the NBO atoms having short Si-O bonds. The distance between oxygen and silicon atoms is sometimes shorter than 1.6 Å in the trajectory of MD simulations with FF-Pedone and FF-Deng, while such short O-Si bonds are rarely observed with FF-Wang. This probably comes from the difference in the properties of NBO atoms between the first two FFs and FF-Wang, in the case of $(\text{SiO}_2)_{0.5}(\text{CaO})_{0.5}$.

Generally, the bonds between Al and O atoms are mainly covalent, and BOs are dominant in $(\text{SiO}_2)_{0.5}(\text{Al}_2\text{O}_3)_{0.5}$ glass. This may be the reason the agreements in $(\text{SiO}_2)_{0.5}(\text{Al}_2\text{O}_3)_{0.5}$ are better than those in $(\text{SiO}_2)_{0.5}(\text{CaO})_{0.5}$, using the first two FFs.

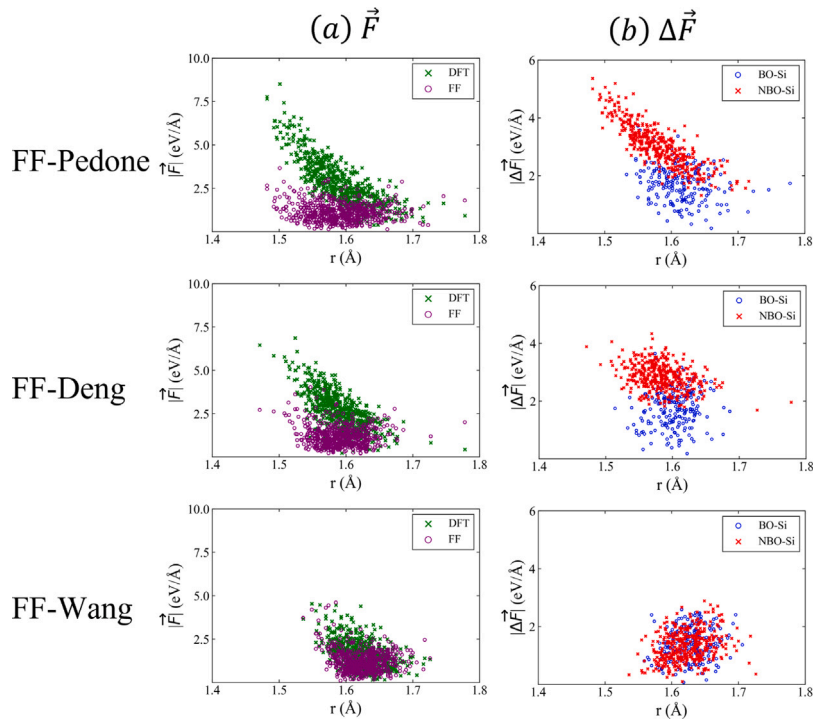


Fig. 2. (a) Comparison of the atomic forces calculated by DFT (green crosses) and classical force fields (purple open circles) for O atoms in $(\text{SiO}_2)_{0.5}(\text{CaO})_{0.5}$. (b) Difference in the two forces for the bridging oxygen (BO) and non-bridging (NBO) oxygen atoms, expressed by blue open circles and red crosses, respectively. In all the figures, the horizontal axis shows the shorter distance of oxygen atoms with the neighboring atoms.

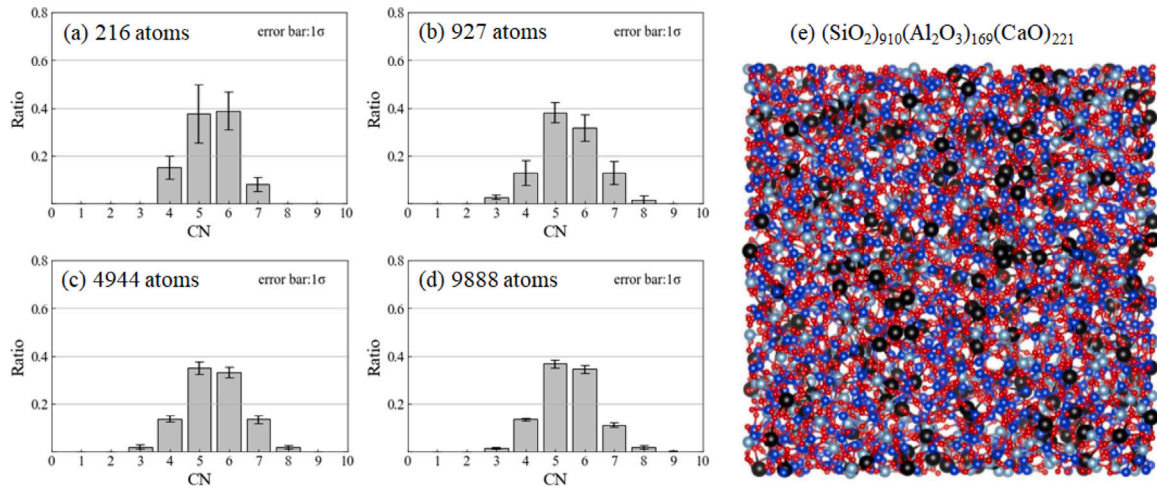


Fig. 3. Distribution of the number of Ca atoms having various coordination numbers in $(\text{SiO}_2)_{0.70}(\text{Al}_2\text{O}_3)_{0.13}(\text{CaO})_{0.17}$ systems, containing (a) 216, (b) 927, (c) 4944, and (d) 9888 atoms. The snapshot structure of the 4944-atom system is shown in (e).

3.2. Large scale DFT calculations of the multicomponent glass systems, $(\text{SiO}_2)_{0.70}(\text{Al}_2\text{O}_3)_{0.13}(\text{XO})_{0.17}$ ($X = \text{Mg}, \text{Ca}, \text{Sr}, \text{Ba}$)

Next, we analyzed the accuracy of classical FFs for more complicated, but widely used multi-component glass systems $(\text{SiO}_2)_{0.70}(\text{Al}_2\text{O}_3)_{0.13}(\text{XO})_{0.17}$ where group II element X is Mg, Ca, Sr, or Ba. Here, we used FF-Pedone because the parameters for various X s are available only with this FF. For such multi-component glasses, the size of the system should be large enough to properly reproduce the actual glass structures. Fig. 3(a)–(d) show the distribution of the coordination number around Ca atoms in the MD simulations for different sizes of the system. This analysis suggests that we need about 5000 atoms to reproduce the correct distribution of the coordination number of Ca atoms. A snapshot structure of MD simulations of $(\text{SiO}_2)_{0.70}(\text{Al}_2\text{O}_3)_{0.13}(\text{CaO})_{0.17}$,

which contains about 5000 atoms, is shown in Fig. 3(e). If the atomic forces depend on the distribution of the coordination numbers, it is important to calculate the electronic structure and atomic forces of such large systems by DFT. As discussed in 2.2, it is very expensive to perform accurate DFT calculations of such large systems using the conventional DFT methods; therefore, we demonstrate here that efficient and reliable calculations are possible with the MSSF method.

Fig. 4 shows the accuracy of the MSSF method in the calculation of vitreous silica glass systems. As explained in Section 2.2.2, the accuracy of the method is controlled by the multisite range, R_{MS} . The total energy of the vitreous silica system containing 999 atoms calculated by the MSSF method using different values of R_{MS} is presented in Fig. 4(a). For this size, the exact value can be evaluated using the primitive PAO basis sets, which is shown by the dotted red line in the figure. These

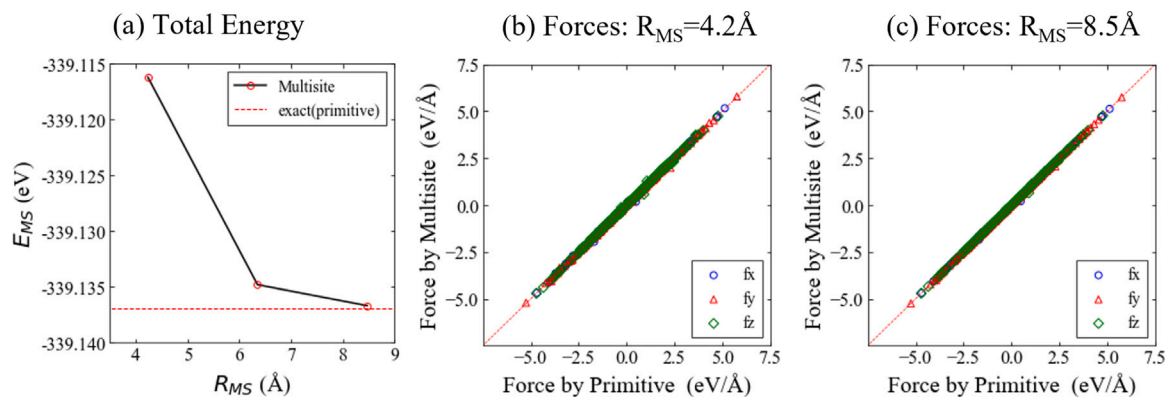


Fig. 4. (a) Total energy of a vitreous silica system containing 999 atoms, calculated by the MSSF method using different multisite range R_{MS} . Comparison of the calculated atomic forces of the snapshot structure using the primitive PAO basis set and the MSSF calculations using (b) $R_{MS} = 4.2$ Å and (c) $R_{MS} = 8.5$ Å.

results show that the MSSF calculation with $R_{MS} = 6.4$ Å is already very accurate. The accuracy of the forces calculated using the MSSF method with $R_{MS} = 4.2$ and 8.5 Å is also investigated, and the results are shown in Fig. 4(b) and (c), respectively. The agreement of the calculated forces by the MSSF method with those using a primitive basis set is almost perfect for both cases.

Next, the DFT calculations of the systems containing about 5000 atoms (Fig. 3(e)) using the MSSF method with $R_{MS} = 8.5$ Å are presented. The results in Fig. 4 show that the calculation with this range of R_{MS} must be highly accurate. It was confirmed that the SCF calculations of such large systems with the MSSF method are stable and robust. The calculations were performed using 9–54 nodes (1 node = 2 CPUs of Xeon Platinum 2.9 GHz, 24 cores) of the Numerical Materials Simulator at NIMS. The elapsed time to converge the SCF charge density and calculate the atomic forces was 6367 s using 9 nodes, and 2298 s using 36 nodes. It is still expensive to perform long-time MD simulations with this timing. However, it should be noted that the elapsed time can be significantly reduced by using $R_{MS} = 4.2$ Å. Furthermore, the number of SCF iterations is expected to be much smaller after the first MD step, since we can begin with the MSSF coefficients and self-consistent charge density obtained in the last MD step. Such an approach will be studied in the future.

The calculated atomic forces are compared with those by FF-Pedone in Fig. 5, showing the $|\Delta F|$ for the BO and NBO atoms. These BO and NBO atoms are further classified by their nearest neighbor atoms, Si or Al. Again, the agreement of the forces between DFT and FF-Pedone are poorer for the NBO atoms than the BO atoms. Furthermore, for the oxygen atoms bonded with Si atoms, the difference in the forces is very large when the distance is shorter than 1.55 Å. This behavior is common for all cases of atom X .

As earlier mentioned, various kinds of local structures can be reproduced in the large-scale structural models containing about 5000 atoms. It is expected that more revised FFs, including the machine-learning FFs, would be developed and applied to such large-scale multi-component glass systems in the future. Here, it is demonstrated that accurate DFT calculations can be performed for the complex glass systems containing more than 5000 atoms, and the accuracy of future FFs can be clarified in detail by such large-scale DFT calculations.

3.3. DFT-MD simulations of $(\text{SiO}_2)_{0.70}(\text{Al}_2\text{O}_3)_{0.13}(\text{XO})_{0.17}$ ($X = \text{Mg}, \text{Ca}, \text{Sr}, \text{Ba}$)

Next, we discuss the MD simulations based on DFT. Although it is possible to perform MD simulations of 5000-atom systems with the MSSF method in principle, it is still expensive. Thus, the DFT-MD simulations of a smaller system $(\text{SiO}_2)_{0.70}(\text{Al}_2\text{O}_3)_{0.13}(\text{CaO})_{0.17}$ containing 927 atoms are performed here. As discussed in the last section, the system size is not large enough to reproduce the distribution of coordination numbers of Ca atoms; however, examples of DFT-MD simulations of glass materials with this size are still rare.

3.3.1. Structural properties of $(\text{SiO}_2)_{0.70}(\text{Al}_2\text{O}_3)_{0.13}(\text{CaO})_{0.17}$

The initial structure for the present DFT-MD simulation was prepared by an NVT-MD simulation with FF-Pedone using the experimental volume. DFT-MD simulations with the fixed volume were performed using a time step of 2.0 fs and the temperature was controlled at 300 K using the stochastic velocity rescaling method [49]. Fig. 6(a) shows the calculated pressure during the simulation. (See Figs. S1 and S2 in Supplementary Material for the temperature and potential energy.) The results show that: (i) the time needed for the equilibration is only about 0.1 – 0.2 ps, and (ii) the calculated internal pressure in the NVT simulation with the experimental volume is about -0.7 GPa, close to 0 GPa. This result suggests that the optimum volume of DFT-MD simulations with GGA is close to the experimental value. If the cell length is reduced by 0.5% , the calculated stress becomes almost 0 GPa, as can be seen by the dotted line in Fig. 6(a). Therefore, DFT-MD simulations based on GGA can reproduce the experimental volume or density, within 1% – 2% . The same procedures are followed for vitreous SiO_2 and $(\text{SiO}_2)_{0.5}(\text{CaO})_{0.5}$ and the calculated stresses are found to be negative and positive, respectively. However, they are both close to 0 GPa, about -3 GPa and $+0.5$ GPa, respectively.

Using the trajectory of the DFT-MD simulations of $(\text{SiO}_2)_{0.70}(\text{Al}_2\text{O}_3)_{0.13}(\text{CaO})_{0.17}$, the structure factor is calculated and shown in Fig. 6(b), together with the experimental result of X-ray scattering, measured at Beamline BL04B2 at SPring-8. The calculated result agrees well with the experimental one in the wide region of wave length Q . The structure factor calculated from a snapshot of NVT-MD simulations with FF-Pedone also reproduces the experimental result. However, it is found that there are also some important differences between the structures from the DFT-MD and MD with FF-Pedone.

Fig. 7 shows the distribution of interatomic distances and bond angles for the snapshot structures obtained by the MD simulation based on DFT and FF-Pedone. For the differences in the bond lengths of Si–O and Al–O, the average lengths by DFT-MD simulations are larger than those from the MD by FF-Pedone. Note that the optimized lattice parameters of crystalline silica and alumina by GGA with the present DZP basis set have an error of about 0.5% , as shown in Table 1. However, the difference in the average bond length between FF-MD and DFT-MD is larger than this value, being about 3% . Furthermore, much clearer differences are observed in the distributions of Si–O–Si angle and Ca–O distance. The average Si–O–Si angle is 140° , in the DFT-MD simulations while it is 160° , in the MD with FF-Pedone. This large difference in the angle distribution may come from the shorter Si–O distance in the MD simulations using FF-Pedone. It may be worth pointing out that there are no peak structures around 90° , which is related to the defect formation of two-membered rings and was discussed in Refs. [50,51].

MD simulations of $(\text{SiO}_2)_{0.70}(\text{Al}_2\text{O}_3)_{0.13}(\text{XO})_{0.17}$ for $X = \text{Mg}, \text{Sr}$ and Ba were also performed. Fig. 7(f)–(h) show the distributions of X –O

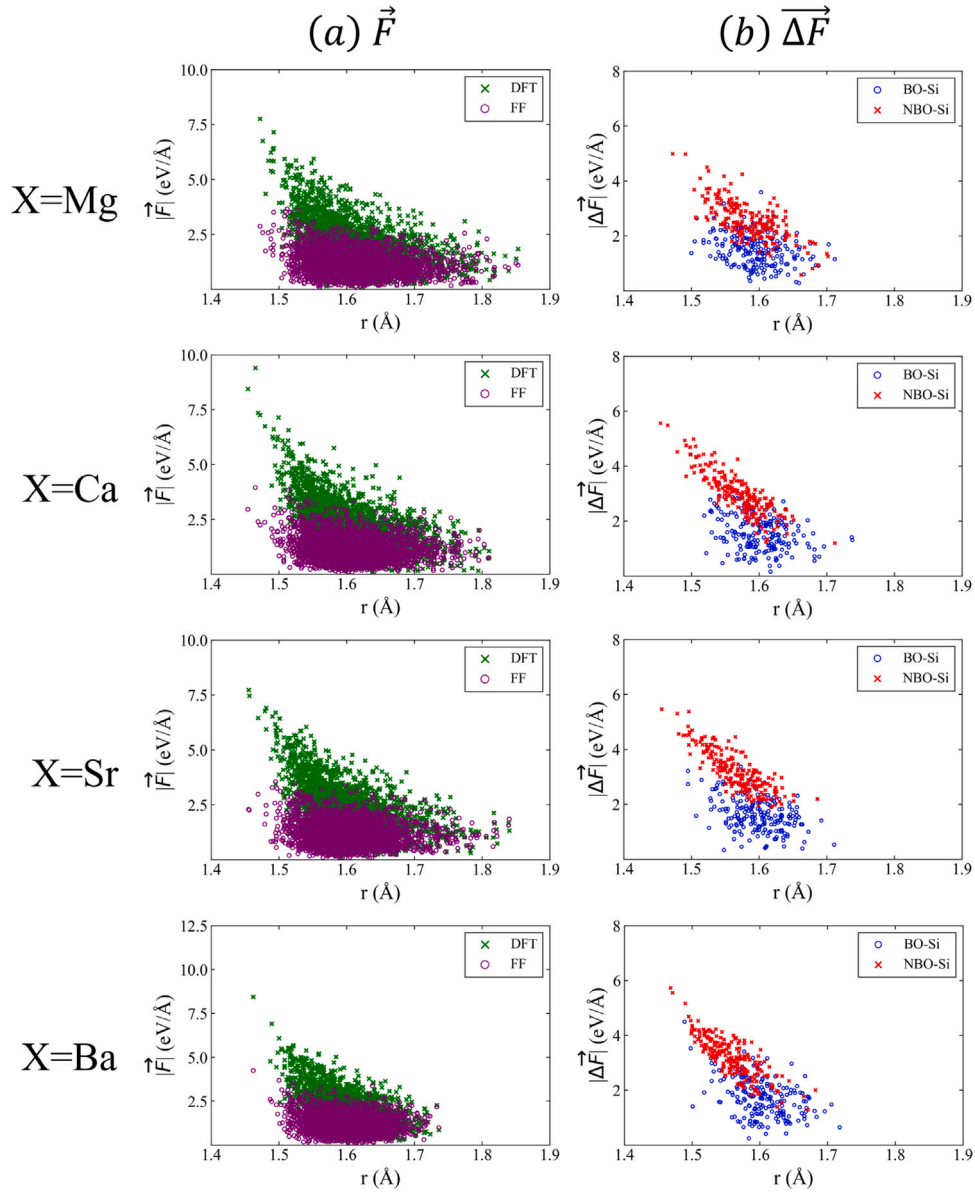


Fig. 5. (a) Comparison of the atomic forces calculated by DFT (green crosses) and classical force fields (purple open circles) for O atoms in $(\text{SiO}_2)_{0.70}(\text{Al}_2\text{O}_3)_{0.13}(\text{XO})_{0.17}$ ($X = \text{Mg}, \text{Ca}, \text{Sr}, \text{Ba}$). (b) Difference in the two forces for the bridging oxygen (BO) and non-bridging oxygen (NBO) atoms are plotted using blue open circles and red crosses, respectively. In (b), 200 atoms are selected randomly for both BO and NBO atoms. In both figures, the horizontal axis shows a shorter distance between oxygen and the neighboring silicon atoms.

distances obtained by MD simulations using DFT and FF-Pedone. In the case of $X = \text{Mg}$, the distribution is similar for the DFT-MD and MD with FF-Pedone simulations, while the X -O distances by the DFT-MD simulations show wider distributions in other cases ($X = \text{Sr}$ or Ba), as can be seen in the Ca case.

3.3.2. Density of states of $(\text{SiO}_2)_{0.70}(\text{Al}_2\text{O}_3)_{0.13}(\text{XO})_{0.17}$ ($X = \text{Mg}, \text{Ca}, \text{Sr}, \text{Ba}$)

The electronic structure of $(\text{SiO}_2)_{0.70}(\text{Al}_2\text{O}_3)_{0.13}(\text{XO})_{0.17}$ was also investigated. As shown in Fig. 8, the total density of states (DOS) for the occupied electrons, ranging from -8 eV to the Fermi level (middle of the band gap), is found to be almost the same for the different X s. In contrast, the DOS for $X = \text{Mg}$ at the unoccupied region near the Fermi level is completely different from those in other cases. Fig. 8(b)–(e) show the projected DOS for Si, Al, O, and X atoms, respectively. The figure shows that the states at the conduction band near the Fermi level mainly comes from X for Ca, Sr, and Ba, but no major contribution from Mg atoms exist in the same region in the case of $X = \text{Mg}$. This

unique electronic property of Mg may be observed in the actual multi-component glass materials; for example, in the absorption spectrum, if there are no other peaks from the impurities in this energy region.

4. Summary

Although molecular dynamics simulations can be a powerful tool to explain the atomic-scale structures of multi-component glass systems, there are several problems to employ reliable and accurate MD simulations of such large and complex materials. The available FFs which can treat many elements are limited and, even if such a FF exists, its accuracy is uncertain due to the large variety and complexity of chemical environments in the multi-component glasses. Although first-principles calculations based on DFT are reliable even for such complex systems, DFT calculations of multi-component systems are difficult because they are large systems containing 1000–5000 atoms or more. Conventional DFT calculations of such large systems are prohibitively expensive.

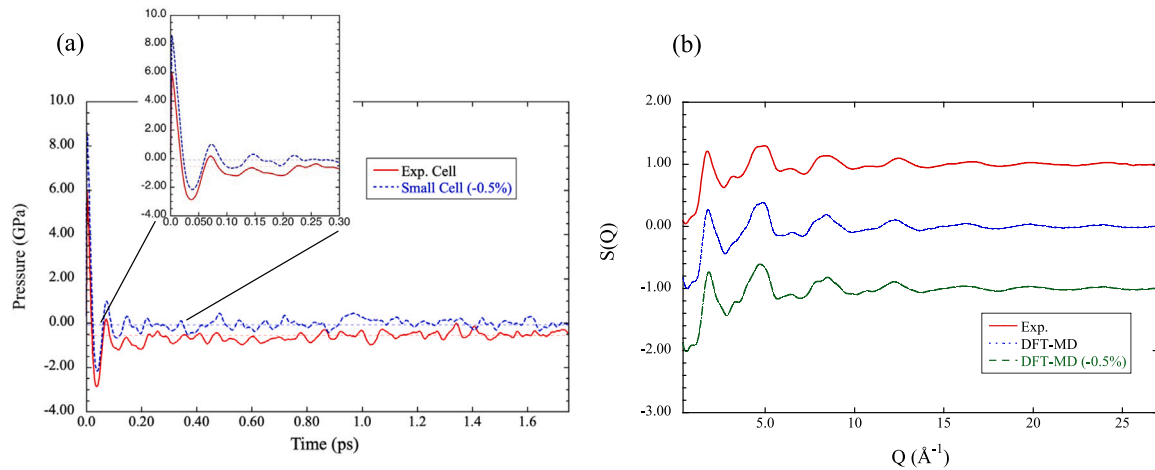


Fig. 6. (a) Calculated pressure during the constant-volume DFT-MD simulations of $(\text{SiO}_2)_{0.70}(\text{Al}_2\text{O}_3)_{0.13}(\text{CaO})_{0.17}$, with the experimental volume and the reduced volume whose cell parameter is reduced by 0.5%. (b) Structure factor calculated from the snapshots of the DFT-MD simulations, with the experimental data for comparison.

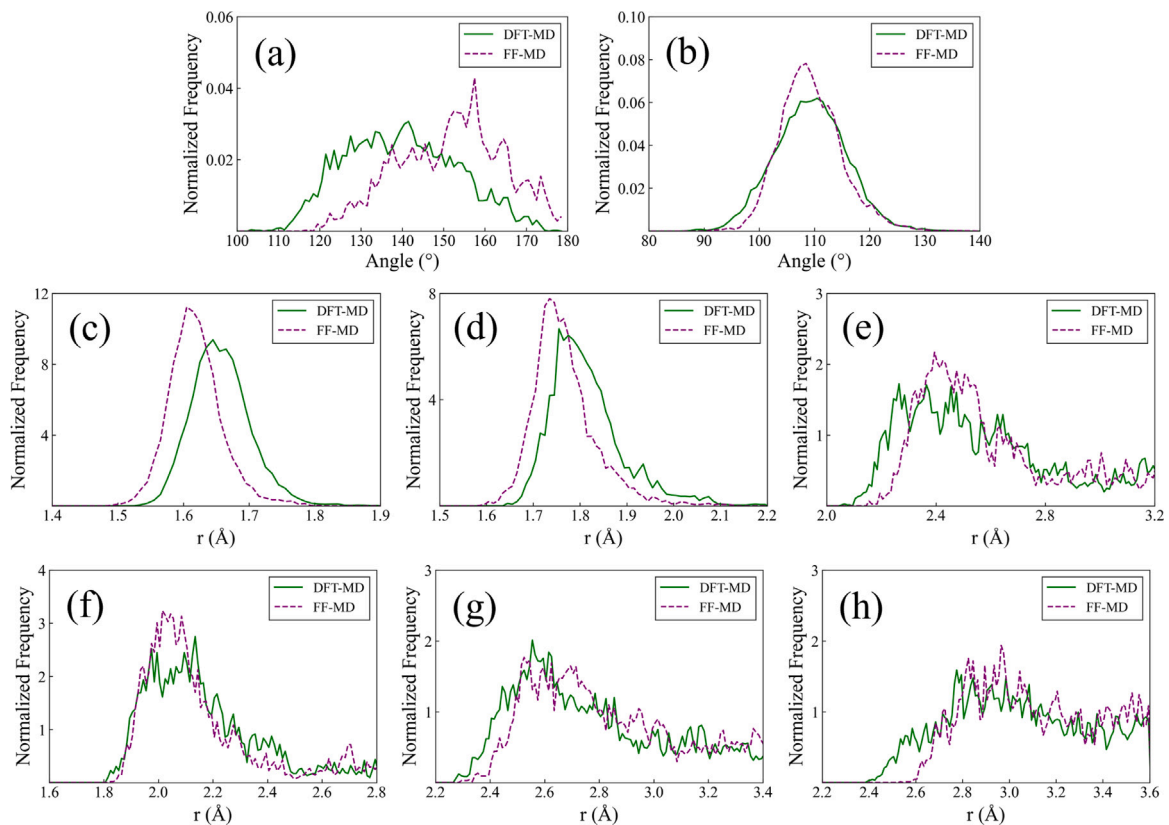


Fig. 7. Comparison of distributions in (a) Si–O–Si angle, (b) O–Si–O angle, (c) Si–O distance, (d) Al–O distance, (e) Ca–O distance, (f) Mg–O distance, (g) Sr–O distance, and (h) Ba–O distance by the DFT-MD and FF-MD models. (a), (b), (c), (d) and (e) are calculated from the snapshot structure of $(\text{SiO}_2)_{0.70}(\text{Al}_2\text{O}_3)_{0.13}(\text{CaO})_{0.17}$, while (f), (g) and (h) are from $(\text{SiO}_2)_{0.70}(\text{Al}_2\text{O}_3)_{0.13}(\text{MgO})_{0.17}$, $(\text{SiO}_2)_{0.70}(\text{Al}_2\text{O}_3)_{0.13}(\text{SrO})_{0.17}$, and $(\text{SiO}_2)_{0.70}(\text{Al}_2\text{O}_3)_{0.13}(\text{BaO})_{0.17}$, respectively.

In this study, we used large-scale DFT techniques with the CONQUEST code to perform a large-scale DFT study of multi-component glasses. The results demonstrated that accurate DFT calculations of multi-component glass systems, $(\text{SiO}_2)_{0.70}(\text{Al}_2\text{O}_3)_{0.13}(\text{XO})_{0.17}$ ($X = \text{Mg}, \text{Ca}, \text{Sr}, \text{Ba}$) containing about 5000 atoms are possible using the multisite method, implemented in the CONQUEST code. Using the results of such large-scale DFT calculations, we have evaluated the accuracy of FF-Pedone, FF-Deng, and FF-Wang for vitreous SiO_2 , $(\text{SiO}_2)_{0.50}(\text{Al}_2\text{O}_3)_{0.50}$, and $(\text{SiO}_2)_{0.50}(\text{CaO})_{0.50}$, and FF-Pedone for $(\text{SiO}_2)_{0.70}(\text{Al}_2\text{O}_3)_{0.13}(\text{XO})_{0.17}$

($X = \text{Mg}, \text{Ca}, \text{Sr}, \text{Ba}$). By analyzing the trajectories of classical MD simulations, it was found that the Si–O distance of the non-bridging oxygen (NBO) atoms is often shorter than 1.55 Å in the simulations using FF-Pedone and FF-Deng, while such short Si–O distances were not observed with FF-Wang. By comparing the forces calculated by FFs and DFT, large deviations from the DFT forces were observed for NBO atoms, specifically for short Si–O bonds, in the case of FF-Pedone and FF-Deng. However, the accuracy of FF-Wang was found to be independent of the difference between NBO and BO atoms. Detailed

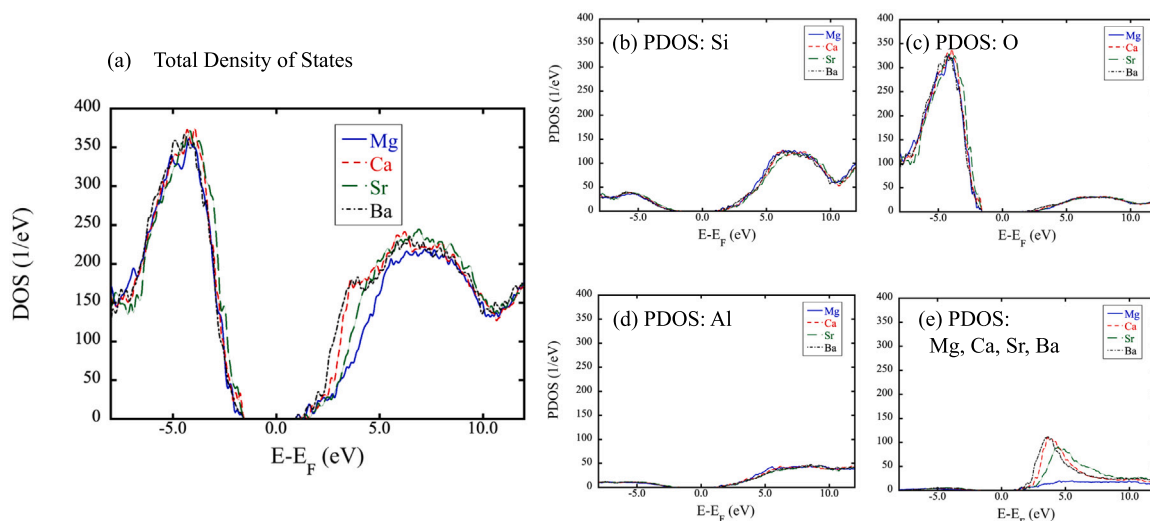


Fig. 8. (a) Total density of states (DOS) of $(\text{SiO}_2)_{0.70}(\text{Al}_2\text{O}_3)_{0.13}(\text{XO})_{0.17}$ ($X = \text{Mg}, \text{Ca}, \text{Sr}, \text{Ba}$) and its projected DOS for (b) Si, (c) O, (d) Al, and (e) X atoms.

comparison of the three FFs shows that they have clear differences when the calculated forces deviate largely from DFT forces. A similar tendency is found for $(\text{SiO}_2)_{0.70}(\text{Al}_2\text{O}_3)_{0.13}(\text{XO})_{0.17}$ ($X = \text{Mg}, \text{Ca}, \text{Sr}, \text{Ba}$) with FF-Pedone. The accuracy of the FF is low for NBO atoms, especially when the distance of Si–O is short.

DFT-MD simulations of about 1000 atom multi-component glass systems were also performed and some significant differences in the distribution of distances and angles between the DFT-MD and FF-MD simulations, specifically around the oxygen atoms. In DFT-MD simulations, smaller angles (Si–O–Si) and larger bond lengths (Si–O) were observed, and as a result of the cancellation, the distance in the Si atoms is almost the same between DFT-MD and FF-MD simulations, both of which used the experimental volume for the simulation cell. For the X –O distances, DFT-MD simulations show wider distributions compared with those FF-MD, except in the case of $X = \text{Mg}$, where the agreement between the two MD simulations is much better.

It was found that the calculated pressure is very low in the DFT-MD simulations using the experimental volume, and the calculated structure factor shows good agreement with the experimental results. Using the snapshot structures obtained by DFT-MD simulations, we also revealed the electronic structure of $(\text{SiO}_2)_{0.70}(\text{Al}_2\text{O}_3)_{0.13}(\text{XO})_{0.17}$ ($X = \text{Mg}, \text{Ca}, \text{Sr}, \text{Ba}$). The analysis of the total and projected DOS (pDOS) shows that the electronic structure in the occupied region is almost the same for the different X s, while the Mg case shows a unique electronic structure in the unoccupied region near the Fermi level.

These results lead to the conclusion that the large-scale DFT methods can be applied to glass systems including multi-component glasses, and can provide various insights, such as the verification of FFs, local structures around specific elements and electronic structure. Many analyses of the mechanical and thermodynamic properties, including free energy profiles using the Blue-moon ensemble [52], can be performed with large-scale DFT techniques, just as with conventional DFT calculations. In the near future, large-scale DFT calculations are expected to make significant contributions to theoretical studies on the detailed structural and physical properties of multi-component glasses.

CRediT authorship contribution statement

Atsushi Tanaka: Investigation, Software, Methodology, Formal analysis, Writing – original draft. **Atsuki Saito:** Conceptualization, Writing – review & editing, Supervision. **Takashi Murata:** Supervision, Project administration. **Ayako Nakata:** Methodology, Software. **Tsuyoshi Miyazaki:** Conceptualization, Methodology, Writing – original draft, Supervision.

Declaration of competing interest

The authors declare that they have no known competing financial interests or personal relationships that could have appeared to influence the work reported in this paper.

Data availability

Data will be made available on request.

Acknowledgments

This work was supported by World Premier International Research Center Initiative (WPI), MEXT, Japan and JSPS Grant-in-Aid for Transformative Research Areas (A) “Hyper-Ordered Structures Science” (JP20H05883). Calculations were performed on the Numerical Materials Simulator at NIMS. The synchrotron radiation experiments were performed at BL04B2 in SPring-8 with the approval of Japan Synchrotron Radiation Research Institute (JASRI) (Proposal No. 2019B2007).

Appendix A. Supplementary data

Supplementary material related to this article can be found online at <https://doi.org/10.1016/j.jnoncrsol.2023.122714>.

References

- [1] J.E. Shelby, *Introduction to glass science and technology*, 2005.
- [2] W.H. Zachariasen, The atomic arrangement in glass, *J. Am. Chem. Soc.* 54 (10) (1932) 3841–3851, <http://dx.doi.org/10.1021/ja01349a006>, arXiv:10.1021/ja01349a006.
- [3] S.R. Elliott, Medium-range structural order in covalent amorphous solids, *Nature* 354 (1991) 445–452, <http://dx.doi.org/10.1038/354445a0>.
- [4] H. Maekawa, T. Maekawa, K. Kawamura, T. Yokokawa, The structural groups of alkali silicate glasses determined from 29Si MAS-nmr, *J. Non-Cryst. Solids* 127 (1) (1991) 53–64, [http://dx.doi.org/10.1016/0022-3093\(91\)90400-Z](http://dx.doi.org/10.1016/0022-3093(91)90400-Z), URL <https://www.sciencedirect.com/science/article/pii/002230939190400Z>.
- [5] C.I. Merzbacher, W.B. White, The structure of alkaline earth aluminosilicate glasses as determined by vibrational spectroscopy, *J. Non-Cryst. Solids* 130 (1) (1991) 18–34, [http://dx.doi.org/10.1016/0022-3093\(91\)90152-V](http://dx.doi.org/10.1016/0022-3093(91)90152-V), URL <https://www.sciencedirect.com/science/article/pii/002230939190152V>.
- [6] A. Pedone, G. Malavasi, M.C. Menziani, A.N. Cormack, U. Segre, A new self-consistent empirical interatomic potential model for oxides, silicates, and silica-based glasses, *J. Phys. Chem. B* 110 (2006) 11780–11795.

- [7] L. Deng, J. Du, Development of boron oxide potentials for computer simulations of multicomponent oxide glasses, *J. Am. Ceram. Soc.* 102 (5) (2019) 2482–2505, <http://dx.doi.org/10.1111/jace.16082>, arXiv:<https://ceramics.onlinelibrary.wiley.com/doi/pdf/10.1111/jace.16082>, URL <https://ceramics.onlinelibrary.wiley.com/doi/abs/10.1111/jace.16082>.
- [8] M. Wang, N. Anoop Krishnan, B. Wang, M.M. Smedskjaer, J.C. Mauro, M. Bauchy, A new transferable interatomic potential for molecular dynamics simulations of borosilicate glasses, *J. Non-Cryst. Solids* 498 (2018) 294–304, <http://dx.doi.org/10.1016/j.jnoncrysol.2018.04.063>, URL <https://www.sciencedirect.com/science/article/pii/S0022309318302643>.
- [9] S. Tsuneyuki, M. Tsukada, H. Aoki, Y. Matsui, First-principles interatomic potential of silica applied to molecular dynamics, *Phys. Rev. Lett.* 61 (1988) 869–872, <http://dx.doi.org/10.1103/PhysRevLett.61.869>, URL <https://link.aps.org/doi/10.1103/PhysRevLett.61.869>.
- [10] B.W.H. van Beest, G.J. Kramer, R.A. van Santen, Force fields for silicas and aluminophosphates based on ab initio calculations, *Phys. Rev. Lett.* 64 (1990) 1955–1958, <http://dx.doi.org/10.1103/PhysRevLett.64.1955>, URL <https://link.aps.org/doi/10.1103/PhysRevLett.64.1955>.
- [11] P. Tangney, S. Scandolo, An ab initio parametrized interatomic force field for silica, *J. Chem. Phys.* 117 (19) (2002) 8898–8904, <http://dx.doi.org/10.1063/1.1513312>, arXiv:[10.1063/1.1513312](https://arxiv.org/abs/10.1063/1.1513312).
- [12] F. Noritake, K. Kawamura, T. Yoshino, E. Takahashi, Molecular dynamics simulation and electrical conductivity measurement of $\text{Na}_2\text{O} \cdot 3\text{SiO}_2$ melt under high pressure; relationship between its structure and properties, *J. Non-Cryst. Solids* 358 (23) (2012) 3109–3118, <http://dx.doi.org/10.1016/j.jnoncrysol.2012.08.027>, URL <https://www.sciencedirect.com/science/article/pii/S0022309312005066>.
- [13] S. Urata, N. Nakamura, T. Tada, H. Hosono, Molecular dynamics study on the co-doping effect of Al_2O_3 and fluorine to reduce Rayleigh scattering of silica glass, *J. Am. Ceram. Soc.* 104 (10) (2021) 5001–5015, <http://dx.doi.org/10.1111/jace.17774>, arXiv:<https://ceramics.onlinelibrary.wiley.com/doi/pdf/10.1111/jace.17774>, URL <https://ceramics.onlinelibrary.wiley.com/doi/abs/10.1111/jace.17774>.
- [14] S. Urata, Modeling short-range and three-membered ring structures in lithium borosilicate glasses using a machine-learning potential, *J. Phys. Chem. C* 126 (50) (2022/12/22) 21507–21517, <http://dx.doi.org/10.1021/acs.jpcc.2c07597>.
- [15] J.C. Fogarty, H.M. Aktulga, A.Y. Grama, A.C.T. van Duin, S.A. Pandit, A reactive molecular dynamics simulation of the silica-water interface, *J. Chem. Phys.* 132 (17) (2010) 174704, <http://dx.doi.org/10.1063/1.3407433>, arXiv:[10.1063/1.3407433](https://arxiv.org/abs/10.1063/1.3407433).
- [16] T. Ohkubo, E. Tsuchida, K. Deguchi, S. Ohki, T. Shimizu, T. Otomo, Y. Iwadate, Insights from ab initio molecular dynamics simulations for a multicomponent oxide glass, *J. Am. Ceram. Soc.* 101 (3) (2018) 1122–1134, <http://dx.doi.org/10.1111/jace.15269>, arXiv:<https://ceramics.onlinelibrary.wiley.com/doi/pdf/10.1111/jace.15269>, URL <https://ceramics.onlinelibrary.wiley.com/doi/abs/10.1111/jace.15269>.
- [17] H. Gong, B. Song, Y. Yang, P. Wang, Z. Cao, X. Chen, G. Zhao, S. Peng, Y. Liu, G. Han, Ab initio molecular dynamics simulation of the structural and electronic properties of aluminoborosilicate glass, *J. Am. Ceram. Soc.* 104 (7) (2021) 3198–3211, <http://dx.doi.org/10.1111/jace.17761>, arXiv:<https://ceramics.onlinelibrary.wiley.com/doi/pdf/10.1111/jace.17761>, URL <https://ceramics.onlinelibrary.wiley.com/doi/abs/10.1111/jace.17761>.
- [18] D.R. Bowler, T. Miyazaki, $\mathcal{O}(\mathcal{N})$ Methods in electronic structure calculations, *Rep. Progr. Phys.* 75 (2012) 36503, <http://dx.doi.org/10.1088/0034-4885/75/3/036503>.
- [19] S. Kohara, J. Akola, H. Morita, K. Suzuya, J.K.R. Weber, M.C. Wilding, C.J. Benmore, Relationship between topological order and glass forming ability in densely packed enstatite and forsterite composition glasses, *Proc. Natl. Acad. Sci.* 108 (36) (2011) 14780–14785, <http://dx.doi.org/10.1073/pnas.1104692108>, arXiv:<https://www.pnas.org/doi/pdf/10.1073/pnas.1104692108>, URL <https://www.pnas.org/doi/abs/10.1073/pnas.1104692108>.
- [20] J. Akola, S. Kohara, K. Ohara, A. Fujiwara, Y. Watanabe, A. Masuno, T. Usuki, T. Kubo, A. Nakahira, K. Nitta, T. Uruga, J.K.R. Weber, C.J. Benmore, Network topology for the formation of solvated electrons in binary $\text{CaO-Al}_2\text{O}_3$ composition glasses, *Proc. Natl. Acad. Sci.* 110 (25) (2013) 10129–10134, <http://dx.doi.org/10.1073/pnas.1300908110>, arXiv:<https://www.pnas.org/doi/pdf/10.1073/pnas.1300908110>, URL <https://www.pnas.org/doi/abs/10.1073/pnas.1300908110>.
- [21] K. Konstantinou, P.V. Sushko, D.M. Duffy, Modelling the local atomic structure of molybdenum in nuclear waste glasses with ab initio molecular dynamics simulations, *Phys. Chem. Chem. Phys.* 18 (2016) 26125–26132, <http://dx.doi.org/10.1039/C6CP03076A>.
- [22] Y. Qian, B. Song, J. Jin, G.I. Prayogo, K. Utimula, K. Nakano, R. Maezono, K. Hongo, G. Zhao, Ab initio molecular dynamics simulation of structural and elastic properties of $\text{SiO}_2\text{-P}_2\text{O}_5\text{-Al}_2\text{O}_3\text{-Na}_2\text{O}$ glass, *J. Am. Ceram. Soc.* 105 (11) (2022) 6604–6615, <http://dx.doi.org/10.1111/jace.18614>, arXiv:<https://ceramics.onlinelibrary.wiley.com/doi/pdf/10.1111/jace.18614>, URL <https://ceramics.onlinelibrary.wiley.com/doi/abs/10.1111/jace.18614>.
- [23] E. Hernández, M.J. Gillan, C.M. Goringe, Linear-scaling density-functional-theory technique: The density-matrix approach, *Phys. Rev. B* 53 (11) (1996) 7147–7157, <http://dx.doi.org/10.1103/PhysRevB.53.7147>.
- [24] D.R. Bowler, T. Miyazaki, M.J. Gillan, Recent progress in linear scaling ab initio electronic structure techniques, *J. Phys.: Condens. Matter* 14 (2002) 2781–2798.
- [25] D.R. Bowler, R. Choudhury, M.J. Gillan, T. Miyazaki, Recent progress with large-scale ab initio calculations: the conquest code, *Phys. Status Solidi (B)* 243 (5) (2006) 989–1000, <http://dx.doi.org/10.1002/pssb.200541386>, arXiv:<https://onlinelibrary.wiley.com/doi/pdf/10.1002/pssb.200541386>, URL <https://onlinelibrary.wiley.com/doi/abs/10.1002/pssb.200541386>.
- [26] A. Nakata, J.S. Baker, S.Y. Mujahed, J.T.L. Poulton, S. Arapan, J. Lin, Z. Raza, S. Yadav, L. Truflandier, T. Miyazaki, D.R. Bowler, Large scale and linear scaling DFT with the CONQUEST code, *J. Chem. Phys.* 152 (16) (2020) 164112, <http://dx.doi.org/10.1063/5.0005074>, arXiv:[10.1063/5.0005074](https://arxiv.org/abs/10.1063/5.0005074).
- [27] J.P. Perdew, K. Burke, M. Ernzerhof, Generalized gradient approximation made simple [Phys. Rev. Lett. 77, 3865 (1996)], *Phys. Rev. Lett.* 78 (1997) 1396, <http://dx.doi.org/10.1103/PhysRevLett.78.1396>, URL <https://link.aps.org/doi/10.1103/PhysRevLett.78.1396>.
- [28] H. Hay, G. Ferlat, M. Casula, A.P. Seitsonen, F. Mauri, Dispersion effects in SiO_2 polymorphs: An ab initio study, *Phys. Rev. B* 92 (2015) 144111, <http://dx.doi.org/10.1103/PhysRevB.92.144111>, URL <https://link.aps.org/doi/10.1103/PhysRevB.92.144111>.
- [29] S. Grimme, Semiempirical GGA-type density functional constructed with a long-range dispersion correction, *J. Comput. Chem.* 27 (15) (2006) 1787–1799, <http://dx.doi.org/10.1002/jcc.20495>.
- [30] E. Hernández, M.J. Gillan, C.M. Goringe, Basis functions for linear-scaling first-principles calculations, *Phys. Rev. B* 55 (20) (1997) 13485–13493, <http://dx.doi.org/10.1103/PhysRevB.55.13485>.
- [31] D.R. Bowler, T. Miyazaki, A. Nakata, L. Truflandier, URL <https://ordern.github.io>.
- [32] D.R. Hamann, URL <https://github.com/pipidog/ONCVSP>.
- [33] D.R. Hamann, Optimized norm-conserving vanderbilt pseudopotentials, *Phys. Rev. B* 88 (2013) 085117, <http://dx.doi.org/10.1103/PhysRevB.88.085117>, URL <https://link.aps.org/doi/10.1103/PhysRevB.88.085117>.
- [34] P. project, URL <http://www.pseudo-dojo.org>.
- [35] M. van Setten, M. Giantomassi, E. Bousquet, M. Verstraete, D. Hamann, X. Gonze, G.-M. Rignanese, The PseudoDojo: Training and grading a 85 element optimized norm-conserving pseudopotential table, *Comput. Phys. Comm.* 226 (2018) 39–54, <http://dx.doi.org/10.1016/j.cpc.2018.01.012>, URL <https://www.sciencedirect.com/science/article/pii/S0010465518300250>.
- [36] J.M. Soler, E. Artacho, J.D. Gale, A. García, J. Junquera, P. Ordejón, D. Sánchez-Portal, The SIESTA method for ab initio order-n materials simulation, *J. Phys.: Condens. Matter* 14 (2002) 2745.
- [37] A.S. Torralba, M. Todorovic, V. Brázdová, R. Choudhury, T. Miyazaki, M.J. Gillan, D.R. Bowler, Pseudo-atomic orbitals as basis sets for the $\mathcal{O}(\mathcal{N})$ DFT code CONQUEST, *J. Phys.: Condens. Matter* 20 (29) (2008) 294206, <http://dx.doi.org/10.1088/0953-8984/20/29/294206>.
- [38] D.R. Bowler, J.S. Baker, J.T.L. Poulton, S.Y. Mujahed, J. Lin, S. Yadav, Z. Raza, T. Miyazaki, Highly accurate local basis sets for large-scale DFT calculations in conquest, *Japan. J. Appl. Phys.* 58 (2019) 100503, <http://dx.doi.org/10.7567/1347-4065/ab45af>.
- [39] L. Levien, C.T. Prewitt, D.J. Weidner, Structure and elastic properties of quartz at pressure, *Am. Mineral.* 65 (1980) 920–930.
- [40] R. Franco, M. Blanco, A. Martín Pendás, E. Francisco, J. Recio, Atomistic simulation of the pressure-temperature-volume diagram in $\alpha\text{-Al}_2\text{O}_3$, *Solid State Commun.* 98 (1) (1996) 41–44, [http://dx.doi.org/10.1016/0038-1098\(96\)00015-4](http://dx.doi.org/10.1016/0038-1098(96)00015-4), URL <https://www.sciencedirect.com/science/article/pii/0038109896000154>.
- [41] B. Gupta, R. Goyal, Static and thermophysical properties of chalcogenide crystals with nacl structure, *Solid State Commun.* 49 (6) (1984) 559–562, [http://dx.doi.org/10.1016/0038-1098\(84\)90191-1](http://dx.doi.org/10.1016/0038-1098(84)90191-1), URL <https://www.sciencedirect.com/science/article/pii/0038109884901911>.
- [42] A. Nakata, D.R. Bowler, T. Miyazaki, Efficient calculations with multisite local orbitals in a large-scale DFT code CONQUEST, *J. Chem. Theory Comput.* 10 (2014) 4813, <http://dx.doi.org/10.1021/ct5004934>.
- [43] A. Nakata, D. Bowler, T. Miyazaki, Optimized multi-site local orbitals in the large-scale DFT program CONQUEST, *Phys. Chem. Chem. Phys.* 17 (2015) 31427, <http://dx.doi.org/10.1039/C5CP00934K>.
- [44] M.J. Rayson, P.R. Briddon, Highly efficient method for Kohn-Sham density functional calculations of 500 – 10000 atom systems, *Phys. Rev. B* 80 (2009) 205104, <http://dx.doi.org/10.1103/PhysRevB.80.205104>.
- [45] M. Rayson, Rapid filtration algorithm to construct a minimal basis on the fly from a primitive Gaussian basis, *Comput. Phys. Comm.* 181 (2010) 1051–1056, <http://dx.doi.org/10.1016/j.cpc.2010.02.012>.
- [46] G.A. Rosales-Sosa, A. Masuno, Y. Higo, H. Inoue, Crack-resistant $\text{Al}_2\text{O}_3\text{-SiO}_2$ glasses, *Sci. Rep.* 6 (1) (2016) 1–7, <http://dx.doi.org/10.1038/srep23620>.

- [47] For $(\text{SiO}_2)_{0.5}(\text{Al}_2\text{O}_3)_{0.5}$, we used 2.78 g/cm^3 which was obtained by a linear interpolation from the experimental densities of the glasses having similar compositions.
- [48] V. Dimitrov, T. Komatsu, Electronic polarizability, optical basicity and non-linear optical properties of oxide glasses, *J. Non-Cryst. Solids* 249 (2) (1999) 160–179, [http://dx.doi.org/10.1016/S0022-3093\(99\)00317-8](http://dx.doi.org/10.1016/S0022-3093(99)00317-8), URL <https://www.sciencedirect.com/science/article/pii/S0022309399003178>.
- [49] G. Bussi, D. Donadio, M. Parrinello, Canonical sampling through velocity rescaling, *J. Chem. Phys.* 126 (2007) 014101, <http://dx.doi.org/10.1063/1.2408420>.
- [50] M. Kim, K.H. Khoo, J.R. Chelikowsky, Simulating liquid and amorphous silicon dioxide using real-space pseudopotentials, *Phys. Rev. B* 86 (2012) 054104, <http://dx.doi.org/10.1103/PhysRevB.86.054104>, URL <https://link.aps.org/doi/10.1103/PhysRevB.86.054104>.
- [51] K. Shirai, K. Watanabe, H. Momida, S. Hyun, First-principles study on the specific heat jump in the glass transition of silica glass and the prigogine-defay ratio, *J. Phys.: Condens. Matter* 35 (50) (2023) 505401, <http://dx.doi.org/10.1088/1361-648X/acf6ec>.
- [52] T. Hirakawa, D.R. Bowler, T. Miyazaki, Y. Morikawa, L.A. Truflandier, Blue moon ensemble simulation of aquation free energy profiles applied to mono and bifunctional platinum anticancer drugs, *J. Comput. Chem.* 41 (22) (2020) 1973–1984, <http://dx.doi.org/10.1002/jcc.26367>.